

Contents

3	Rayleigh-Bénard convection	1
3.1	Governing equations	1
3.2	Nondimensionalisation and scale analysis	2
3.3	Hyperdiffusion terms	3
3.4	Model configuration	4
3.5	Choice of resolution: literature	4
3.5.1	Resolution guidelines	4
3.5.2	Metrics sensitive to under-resolution	5
3.6	Choice of resolution: experiment	6

This page intentionally left blank

Talia flammato secum dea corde volutans
nimborum in patriam, loca feta furentibus austris,
Aeoliam venit. Hic vasto rex Aeolus antro
luctantes ventos tempestatesque sonoras
imperio premit ac vinclis et carcere frenat.
Illi indignantes magno cum murmure montis
circum claustra fremunt; celsa sedet Aeolus arce
sceptra tenens, mollitque animos et temperat iras.
Ni faciat, maria ac terras caelumque profundum
quippe ferant rapidi secum verrantque per auras.
Sed pater omnipotens speluncis abdidit atris,
hoc metuens, molemque et montis insuper altos
imposuit, regemque dedit, qui foedere certo
et premere et laxas sciret dare iussus habenas.

Thus inwardly brooding with heart inflamed,
the goddess came to Aeolia, motherland of
storm clouds, tracts teeming with furious
blasts. Here in his vast cavern, Aeolus, their
king, keeps under his sway and with prison
bonds curbs the struggling winds and the roar-
ing gales. They, to the mountain's mighty
moans, chafe blustering around the barriers.
In his lofty citadel sits Aeolus, sceptre in hand,
taming their passions and soothing their rage;
did he not so, they would surely bear off with
them in wild flight seas and lands and the
vault of heaven, sweeping them through space.
But, fearful of this, the father omnipotent hid
them in gloomy caverns, and over them piled
high mountain masses and gave them a king
who, under fixed covenant, should be skilled
to tighten and loosen the reins at command.

Virgil, *Aeneid* I, ll. 50–63
trans. H. R. Fairclough

Chapter 3

Rayleigh-Bénard convection

Having established a useful set of tools and identified directions for further work in the previous chapter's review of the Lorenz '96 literature, I now propose to use two-dimensional Rayleigh-Bénard convection as an intermediate-complexity test problem for data-driven parametrisation. §§ 3.1–3.4 first cover the governing equations and the numerical methods used to solve them. §§ 3.5 and 3.6 then take the important step of choosing the spatial resolutions of the models used for data-driven parametrisation, first reviewing relevant literature and then performing numerical experiments.

3.1 Governing equations

Rayleigh-Bénard convection is the overturning motion of a fluid confined between two horizontal isothermal plates, the bottom plate being warmer than the top plate. The fluid is traditionally assumed to be incompressible, with density ρ related to temperature T by the linear equation of state

$$\rho = \rho_0[1 - \alpha(T - T_0)],$$

α being the volume coefficient of thermal expansion and ρ_0 and T_0 a reference density and temperature. Provided that the density variations are small ($\alpha(T - T_0) \ll 1$), one may employ the *Boussinesq approximation*, neglecting density variations everywhere except in their contribution to the weight force. This leads to the Boussinesq equations

$$\frac{\partial \mathbf{u}}{\partial t} + \mathbf{u} \cdot \nabla \mathbf{u} = -\frac{1}{\rho_0} \nabla p' + \alpha(T - T_0)g\hat{\mathbf{z}} + \nu \nabla^2 \mathbf{u}, \quad (3.1)$$

$$\frac{\partial T}{\partial t} + \mathbf{u} \cdot \nabla T = \kappa \nabla^2 T, \quad \text{and} \quad (3.2)$$

$$\nabla \cdot \mathbf{u} = 0, \quad (3.3)$$

which represent the momentum balance, the conservation of energy and the assumption of incompressibility, respectively. The prognostic variables are the fluid velocity \mathbf{u} and the temperature T (the pressure

perturbation p' is implicitly determined by (3.3)). The parameters of the model are the kinematic viscosity ν and thermal diffusivity κ . $\hat{\mathbf{z}}$ is the upward unit vector. The Boussinesq approximation has led to the appearance of a buoyant force (per unit mass)

$$\alpha(T - T_0)g = \frac{\rho_0 - \rho}{\rho_0}g$$

in the momentum equation, in agreement with Archimedes' principle. The reader is referred to Chandrasekhar (1961) for a detailed derivation of the Boussinesq equations; I have merely summarised the main assumptions and approximations involved.

In this work, I consider solutions of (3.1)–(3.3) in a two-dimensional domain $[0, d] \times [0, L]$ with Cartesian coordinates x and z , subject to no-slip, isothermal boundary conditions

$$\mathbf{u} = \mathbf{0}, \quad T = T_0 + \frac{\delta T}{2} \quad \text{at } z = 0 \text{ and} \quad (3.4)$$

$$\mathbf{u} = \mathbf{0}, \quad T = T_0 - \frac{\delta T}{2} \quad \text{at } z = d \quad (3.5)$$

on the top and bottom plates, and periodic boundary conditions

$$\mathbf{u}(x = 0) = \mathbf{u}(x = L) \quad \text{and} \quad T(x = 0) = T(x = L) \quad (3.6)$$

in the horizontal. δT is the constant temperature difference between the plates.

3.2 Nondimensionalisation and scale analysis

It is helpful to nondimensionalise the governing equations (3.1)–(3.6); this is not only useful for numerical work but also gives insight into the different flow regimes that are possible. A range of nondimensionalisations are used in fluid dynamics literature; I adopt a common one (see, e.g., Grötzbach 1983; Ouertatani et al. 2008; Stevens, Verzicco, and Lohse 2010) which is suitable for the turbulent convective regime.

The first step is to choose representative time, length and temperature scales. For low-viscosity, turbulent flow, a suitable timescale is the *free-fall time* t_0 , which is the time for a fluid element with constant temperature $T = T_0 - \delta T$ to fall from the top plate to the bottom plate under the influence of buoyancy ($-g\alpha\delta T$) alone. It is simple to show that

$$t_0 \sim \left(\frac{d}{g\alpha\delta T} \right)^{1/2},$$

ignoring a factor of $\sqrt{2}$. The obvious length and temperature scales are the plate separation d and temperature difference δT , respectively.

Making the substitutions $p'/\rho_0 \rightarrow \pi$ and $T - T_0 \rightarrow \theta$ in (3.1)–(3.6) and expressing all variables in units of t_0 , d and δT leads to the dimensionless equations

$$\frac{\partial \mathbf{u}}{\partial t} + \mathbf{u} \cdot \nabla \mathbf{u} = -\nabla \pi + \left(\frac{\text{Pr}}{\text{Ra}} \right)^{1/2} \nabla^2 \mathbf{u} + \theta \hat{\mathbf{z}}, \quad (3.7)$$

$$\frac{\partial \theta}{\partial t} + \mathbf{u} \cdot \nabla \theta = (\text{Ra Pr})^{-1/2} \nabla^2 \theta, \quad \text{and} \quad (3.8)$$

$$\nabla \cdot \mathbf{u} = 0, \quad (3.9)$$

which are solved in the domain $[0, \Gamma] \times [0, 1]$ with boundary conditions

$$\mathbf{u} = \mathbf{0}, \quad \theta = +\frac{1}{2} \quad \text{at } z = 0, \quad (3.10)$$

$$\mathbf{u} = \mathbf{0}, \quad \theta = -\frac{1}{2} \quad \text{at } z = 1, \quad (3.11)$$

$$\mathbf{u}(x = 0) = \mathbf{u}(x = \Gamma) \quad \text{and} \quad \theta(x = 0) = \theta(x = \Gamma). \quad (3.12)$$

There are three dimensionless parameters: the aspect ratio of the domain

$$\Gamma \equiv \frac{L}{d},$$

the *Prandtl number*

$$\text{Pr} \equiv \frac{\nu}{\kappa}$$

which measures the relative importance of viscosity (momentum diffusivity) and thermal diffusivity, and the *Rayleigh number*

$$\text{Ra} \equiv \frac{g\alpha d^3 \delta T}{\kappa\nu}.$$

The Rayleigh number can be interpreted as the ratio of the timescale for thermal transport by conduction to the timescale for thermal transport by convection. It determines the importance of diffusion for the evolution of \mathbf{u} and θ ; inspection of (3.7) and (3.8) indicates that low Ra implies strong diffusion and high Ra weak diffusion. Stability analysis (see, e.g., Chandrasekhar (1961) and the seminal work by Lord Rayleigh (1916)) reveals that there exists a critical Rayleigh number (dependent on boundary conditions but of order 10^3), below which the equations have a stable equilibrium with the fluid at rest and a linear conductive temperature profile. Above the critical Rayleigh number, the equilibrium is unstable and small perturbations lead to the formation of a regular series of steady convection cells. If the Rayleigh number is increased much further (Le Quéré (1991) cites $\text{Ra} \approx 2 \times 10^8$), the solution becomes unsteady and increasingly turbulent. This work is concerned with the turbulent regime, since Rayleigh numbers for atmospheric deep moist convection can be as large as 10^{22} (Chillà and Schumacher 2012).

3.3 Hyperdiffusion terms

In Chapter 5 I will compare the output of a parametrised low-resolution model of (3.1)–(3.12) to the output of the unparametrised base model (i.e., the control). However, it was found in the early stages of this work that unparametrised low-resolution models were prone to numerical instability, preventing the obtainment of a suitable control solution. This is to be expected; at high Rayleigh numbers, when dissipation is weak, the solutions develop large gradients near small-scale features that cannot be properly resolved by coarse models, causing the model to crash. To be more precise, the energy spectra of turbulent flows exhibit an *energy cascade* whereby energy is transferred from larger-scale motions to smaller-scale motions; only at sufficiently small scales is energy removed from the system by the dissipative terms in the equations (Pope 2000). In coarse models where these smallest scales are not resolved, excess energy accumulates at the highest resolved wavenumbers.

I choose to stabilise the numerical model by introducing artificial dissipative terms that act on the smallest scales. The modified equations, with the new terms highlighted in red, are

$$\frac{\partial \mathbf{u}}{\partial t} + \mathbf{u} \cdot \nabla \mathbf{u} = -\nabla \pi + \left(\frac{\text{Pr}}{\text{Ra}} \right)^{1/2} (\nabla^2 \mathbf{u} + \tilde{\nu} f(z) |\nabla^2 \mathbf{u}| \nabla^2 \mathbf{u}) + \theta \hat{\mathbf{z}}, \quad (3.13)$$

$$\frac{\partial \theta}{\partial t} + \mathbf{u} \cdot \nabla \theta = (\text{Ra Pr})^{-1/2} (\nabla^2 \theta + \tilde{\kappa} f(z) |\nabla^2 \theta| \nabla^2 \theta), \quad \text{and} \quad (3.14)$$

$$\nabla \cdot \mathbf{u} = 0, \quad (3.15)$$

where the constants $\tilde{\nu} = \tilde{\kappa} = 2 \times 10^{-3}$ were chosen by trial and error to achieve sufficient dissipation. The function $f(z)$ is necessary to reduce the artificial terms to zero near the top and bottom of the domain (otherwise the model crashes) while leaving them relatively unchanged in the interior, and is defined by

$$f(z) = \left[1 - \exp \left(-\frac{\min(z, 1-z)}{0.052} \right) \right]^4.$$

The definition of $f(z)$ is inspired by the *van Driest damping function* commonly used in large-eddy simulations of wall-bounded flows (Pope 2000).

The new additions are akin to regular viscous and diffusive terms with viscosity and diffusivity coefficients that depend on second derivatives of the flow variables. Small-scale features, where $|\nabla^2 \mathbf{u}|$ and/or $|\nabla^2 \theta|$ are large, will experience a larger effective viscosity and/or thermal diffusivity respectively, and therefore be dissipated more rapidly than larger-scale features.

It must be emphasised that this work is *not* concerned with whether these modified equations are an accurate representation of physical reality; they simply serve as an example dynamical system for the study of parametrisation.

3.4 Model configuration

The nondimensionalised Boussinesq equations (3.13)–(3.15) and (3.10)–(3.12) are solved numerically using Dedalus (v3), a spectral code built in Python (Burns et al. 2020). Spectral methods represent the solution of a partial differential equation as a linear combination of linearly independent basis functions, solving for the coefficients of the basis function expansion rather than the values of the solution in real space. The resolution of the model is thus set by choosing the number of basis functions used. This work uses a Fourier (sine/cosine) basis in the horizontal direction and a basis of Chebyshev polynomials (of the first kind) in the vertical direction. The Fourier basis has the special property that all linear combinations respect the periodic boundary conditions. For storage and analysis, the model output is transformed into real space, where the fields are defined on a *collocation grid* that has uniform horizontal spacing but non-uniform vertical spacing (smaller near the top and bottom of the domain and larger in the middle).

Timestepping is performed using a second-order Runge-Kutta scheme. The Rayleigh number was set to 10^9 , a value at which the flow was found to be unsteady and feature transient eddies. The aspect ratio of the domain was $\Gamma = 8$ and the Prandtl number was set to 1 for simplicity. The complete model source code is publicly available; see [Appendix A](#).

3.5 Choice of resolution: literature

The next important step is to choose the resolution of the fine and coarse models that will be used in the data-driven parametrisation process. The fine model will serve as “truth”, providing the training dataset to which the parametrisation model will be fitted and the test dataset against which the parametrised coarse model will be evaluated. Its resolution should therefore be high enough that the (yet-to-be-)chosen evaluation metrics are relatively insensitive to small changes in resolution (i.e., there should be near-convergence of long-term statistics). Note, however, that neither a perfect solution of the fluid equations nor perfect agreement with real-world experimental measurements are necessary; the fine model merely serves as a reference dynamical system whose behaviour I aim to reproduce by parametrising the coarse model. In order to create a worthwhile parametrisation problem, the coarse model’s resolution should therefore be low enough that it exhibits statistically significant biases relative to the fine model, as measured by the chosen evaluation metrics. However, as explained in § 3.3, the coarse model must still be numerically stable so that it can provide an unparametrised control solution.

With the above constraints in mind, § 3.5.1 will review the guidelines that have been established in the literature for producing well-resolved simulations of Rayleigh-Bénard convection. § 3.5.2 will then review the metrics that are known to be sensitive to under-resolution; these may be used to experimentally determine appropriate resolutions for the fine and coarse models, and later (in [Chapter 5](#)) to evaluate parametrisation performance.

3.5.1 Resolution guidelines

Grötzbach (1983) is recognised as the first to formulate resolution requirements for accurate simulations of Rayleigh-Bénard convection (Chillà and Schumacher 2012; Scheel, Emran, and Schumacher 2013). He

identified separate constraints on the mean (i.e., averaged in each spatial direction) grid spacing and the vertical spacing near the plates; I first discuss the former. Grötzbach reasoned that a numerical model that neglects subgrid-scale effects must have a geometric mean grid spacing h (i.e. $h = (\Delta x \Delta y \Delta z)^{1/3}$ in 3D) such that

$$h \leq \underbrace{\pi \left(\frac{\text{Pr}}{\text{Ra}} \right)^{3/8} \langle \epsilon_k \rangle^{-1/4}}_{\eta}, \quad (3.16)$$

where η is the *Kolmogorov length*, the universal smallest relevant length scale for general turbulent flow, and $\langle \epsilon_k \rangle$ is the spatial and temporal average of the kinetic energy dissipation rate defined by

$$\epsilon_k(\mathbf{x}, t) \equiv \frac{1}{2} \left(\frac{\text{Pr}}{\text{Ra}} \right)^{1/2} \sum_{ij} \left(\frac{\partial u_i}{\partial x_j} + \frac{\partial u_j}{\partial x_i} \right)^2 \quad (3.17)$$

(Chillà and Schumacher 2012). The inequality (3.16) between h and η can be understood using the Nyquist-Shannon theorem, which states that a sampling frequency $f \geq k/\pi$ is needed to unambiguously reconstruct a signal with maximum wavenumber k ; substituting $f = 1/h$, $k = 1/\eta$ leads to the claimed relation.

Grötzbach recognised that the above reasoning was only valid for the mean grid spacing; large gradients in temperature and velocity near the top and bottom plates require finer resolution in those regions. The notion of nearness can be formalised by considering the thickness of the *thermal boundary layer*, the region at each plate where large temperature gradients exist. Consider a Taylor series expansion of the horizontally- and time-averaged dimensionless temperature profile about $z = 0$; recalling the boundary condition (3.10), this reads

$$\langle \theta \rangle_{A,t} \approx \frac{1}{2} + \left. \frac{\partial \langle \theta \rangle_{A,t}}{\partial z} \right|_{z=0} z + O(z^2).$$

The thermal boundary layer thickness δ_θ is defined (see, e.g., Chillà and Schumacher 2012) as the height at which, to first order, the temperature reaches the mean value in the well-mixed interior of the domain (i.e., zero for this problem). It follows that

$$\delta_\theta = -\frac{1}{2} \left(\left. \frac{\partial \langle \theta \rangle_{A,t}}{\partial z} \right|_{z=0} \right)^{-1}. \quad (3.18)$$

And similarly for the other boundary layer at $z = 1$. One then asks how many grid points must be within the thermal boundary layer. Grötzbach claimed that 3 points are sufficient for turbulent flows but did not give a theoretical argument to derive this number. Shishkina et al. (2010) presented a theoretical argument based on the (experimentally and numerically justified) assumption of laminar *Prandtl-Blasius* flow conditions in the boundary layer and were able to calculate the minimum number of grid points (e.g., 9 for $\text{Ra} = 2 \times 10^9$ and $\text{Pr} = 0.7$). The results agreed with criteria derived in previous numerical experiments. Importantly, the results of Shishkina et al. allow *a priori* determination of vertical resolution requirements, potentially bypassing the time-consuming and expensive process of iteratively running simulations, checking their convergence and updating the resolution.

3.5.2 Metrics sensitive to under-resolution

Performing numerical experiments for a 3D fluid layer, Grötzbach found that the RMS velocity and the *Nusselt number* were the most sensitive quantities to insufficient mean grid spacing, but even they increased “only slightly” above the values obtained from well-resolved simulations. The dimensionless Nusselt number measures the instantaneous rate of (vertical) heat transport across a horizontal plane at height z , normalised by the purely conductive rate that would exist if the fluid were at rest (Verzicco and Camussi 1999). Following Kooij et al. (2018), I define

$$\text{Nu}(z, t) \equiv \sqrt{\text{Ra Pr}} \langle w \theta \rangle_A - \left\langle \frac{\partial \theta}{\partial z} \right\rangle_A$$

where $\langle \cdot \rangle_A$ denotes averaging over the horizontal plane at height z , and $w = \mathbf{u} \cdot \hat{\mathbf{z}}$ is the vertical velocity. Notice that the heat transport has contributions from both advection (the first term) and conduction (the second term). Authors frequently consider the vertically-averaged value

$$\langle \text{Nu}(z, t) \rangle_z = \sqrt{\text{Ra Pr}} \langle w \theta \rangle_{A,z} + 1 \quad (3.19)$$

and/or the time-averaged value, which is independent of height due to energy conservation,

$$\langle \text{Nu}(z, t) \rangle_t = \langle \text{Nu}(z, t) \rangle_{z,t} = \sqrt{\text{Ra Pr}} \langle w \theta \rangle_{A,z,t} + 1.$$

Later work also supports the finding that the Nusselt number is sensitive to under-resolution. Even studying only steady-state convective solutions at moderate Rayleigh number, Le Quéré (1991) found that the maximum and minimum Nusselt numbers were most sensitive to changes in resolution and had the largest uncertainty among existing benchmark solutions. Other studies have used the convergence of the Nusselt number as an indicator that the spatial resolution is sufficient to produce an accurate solution (Ouertatani et al. 2008).

Stevens, Verzicco, and Lohse (2010) performed 3D simulations in a finite cylindrical cavity with the aim of reconciling the apparent disagreement between the Nusselt numbers in previous numerical studies and experimental observations. They found that agreement with experiment could be achieved, but only by using a much higher resolution than the previous studies. They offered the physical explanation that horizontally under-resolved simulations produce insufficient thermal diffusion, leading to systematic overestimation of the buoyancy of convective plumes near the side-walls of the cylinder; this results in Nusselt numbers that exceed experimentally observed values. This led them to conclude that the two criteria of Grötzsch (1983)—for mean grid spacing and for the vertical spacing near the upper and lower plates—are not independent; the definition $h = (\Delta x \Delta y \Delta z)^{1/3}$ in (3.16) allows the horizontal spacing to remain relatively coarse near the plates, provided the vertical spacing is small. Since fine horizontal resolution is also necessary to accurately capture the dynamics of the thin plumes, they proposed that (3.16) be applied with $h = \max(\Delta x, \Delta y, \Delta z)$ instead.

Some more recent work, however, casts doubt on the notion that the Nusselt number is sensitive to under-resolution and that its convergence is a good indicator that the flow is well-resolved. In assessing the performance of several published computational fluid dynamics codes on the Rayleigh-Bénard problem in a cylindrical cavity, Kooij et al. (2018) identified one higher-order code that reproduced the theoretically predicted scaling of Nu as a function of Ra even when the flow was deliberately under-resolved. On the other hand, the presence of numerical artefacts in the instantaneous temperature field near the bottom plate was a clear indicator of insufficient resolution.

Scheel, Emran, and Schumacher (2013) performed similar high-resolution simulations for a cylindrical cavity and also found that the Nusselt number, among other global transport properties, were “fairly insensitive to insufficient resolution, as long as the mean Kolmogorov length [was] resolved” (i.e., (3.16) was satisfied). However, they found that the horizontally averaged or local kinetic energy dissipation rate (3.17) and the corresponding thermal dissipation rate

$$\epsilon_\theta(\mathbf{x}, t) \equiv (\text{Ra Pr})^{-1/2} \sum_i \left(\frac{\partial \theta}{\partial x_i} \right)^2 \quad (3.20)$$

were much more sensitive, with their convergence requiring even stricter conditions than (3.16).

3.6 Choice of resolution: experiment

I have performed a series of simulations at different resolutions using the numerical model described in § 3.4, using the metrics identified in § 3.5.2 to determine appropriate resolutions for the fine and coarse models in the parametrisation study of Chapters 4 and 5. The coarsest simulation had a resolution of 256 horizontal (Fourier) modes by 64 vertical (Chebyshev) modes and the highest 2048 by 256.

Higher-resolution simulations require shorter time steps in order to be stable. The suitability of the time step is determined by the *Courant number* (Pope 2000)

$$C \equiv \frac{|u|}{\Delta x/\Delta t} + \frac{|w|}{\Delta z/\Delta t},$$

which expresses the horizontal and vertical velocities u and w in units of the grid spacings¹ Δx and Δz per time step Δt , and must be sufficiently small (typically less than 1). The time step was tuned by trial and error at an intermediate starting resolution (not shown) and the time step for other resolutions was scaled to approximately preserve C . The scaling is derived by reasoning that, if $|u|$ and $|w|$ are approximately equal on average and independent of resolution, then for two simulations denoted by subscripts 1 and 2, the equality of C_1 and C_2 implies

$$\begin{aligned} \frac{1}{\Delta x_1/\Delta t_1} + \frac{1}{\Delta z_1/\Delta t_1} &= \frac{1}{\Delta x_2/\Delta t_2} + \frac{1}{\Delta z_2/\Delta t_2} \\ \Leftrightarrow \quad \Delta t_2 &= \frac{1/\Delta x_1 + 1/\Delta z_1}{1/\Delta x_2 + 1/\Delta z_2} \Delta t_1. \end{aligned}$$

Recognising that the grid spacings are related to the numbers of grid points (or spectral modes) N_x and N_z by $\Delta x = \Gamma/N_x$ and $\Delta z \approx 1/N_z$ (where Γ is the aspect ratio of the domain), this may be further simplified to

$$\Delta t_2 = \frac{N_{x_1}/\Gamma + N_{z_1}}{N_{x_2}/\Gamma + N_{z_2}} \Delta t_1.$$

Table 3.1 summarises the resolutions of the simulations and their time steps.

N_x	N_z	Δt
256	64	5.333×10^{-3}
512	64	4×10^{-3}
768	96	2.667×10^{-3}
1024	128	2×10^{-3}
1280	160	1.6×10^{-3}
1536	192	1.333×10^{-3}
1792	224	1.143×10^{-3}
2048	256	1×10^{-3}

Table 3.1: Resolutions and time steps of the simulations used in the resolution-dependence experiment.

The simulations with resolution 1024×128 and coarser were started from the initial condition described in Appendix B.1 and run for 1000 time units. The simulations with resolution finer than 1024×128 were initialised by interpolating the 1024×128 solution at time $t = 650$ and run for a further 350 time units to reduce computational cost. All output was saved at an interval of approximately 0.2 time units. The first 750 time units of data were discarded to ensure that all simulations had reached a statistically steady state (Appendix B.2 verifies this).

For each simulation, I calculated time averages of the following quantities:

- The vertically-averaged Nusselt number $\langle \text{Nu}(z, t) \rangle_z$, defined by (3.19),
- The horizontally-averaged thickness of the two thermal boundary layers $(\langle \delta_{\theta, z=0} \rangle_x + \langle \delta_{\theta, z=1} \rangle_x)/2$, defined by (3.18),
- The RMS speed $\sqrt{\langle \mathbf{u} \cdot \mathbf{u} \rangle_{x,z}}$,
- The domain-averaged kinetic energy dissipation rate $\langle \epsilon_k \rangle_{x,z}$, defined by (3.17), and

¹Since the model uses a spectral method, Δx and Δz are taken to be the local spacings of the collocation grid in real space; see § 3.4.

- e. The domain-averaged thermal dissipation rate $\langle \epsilon_\theta \rangle_{x,z}$, defined by (3.20).

Time averaging was performed over the 250 time units of data that remained after discarding the first 750. I identified two related dominant sources of uncertainty in the calculated values: (i) the uncertainty due to the finite averaging time and (ii) the uncertainty arising from low-frequency fluctuations of the quantities being averaged (i.e., the fact that the results change if the finite averaging window is translated in time). I estimated (i) as half the range of the running mean,

$$\frac{1}{2} \text{range}_{\tau \in [150, 250]} \frac{1}{\tau} \int_{750}^{750+\tau} (\cdot) dt, \quad (3.21)$$

which measures the sensitivity of the result to changes in the averaging time. I estimated (ii) as half the range of the 150-time-unit rolling mean,

$$\frac{1}{2} \text{range}_{\tau \in [0, 100]} \frac{1}{150} \int_{750+\tau}^{900+\tau} (\cdot) dt, \quad (3.22)$$

which measures the sensitivity of the result to the translation of the averaging window. I took the larger of (3.21) and (3.22) as a conservative estimate of the overall uncertainty.

Figure 3.1 shows plots of the five metrics as functions of resolution, expressing the values as percentage errors relative to the highest-resolution simulation. Firstly, observe that all the metrics (except perhaps the RMS speed) appear insensitive to small changes in resolution about 2048×256 ; I therefore choose 2048×256 as the resolution of the fine “truth” model for the parametrisation study.

All five metrics exhibit statistically significant discrepancies across the range of resolutions tested. I choose 256×64 as the resolution of the coarse model for the parametrisation study because it produces the largest error for all metrics while remaining numerically stable.

Notice also that the Nusselt number (Figure 3.1a) and thermal boundary layer thickness (Figure 3.1b) have both a monotonic resolution dependence and small relative uncertainties. This will make them reliable metrics for evaluating parametrisation performance in Chapter 5.

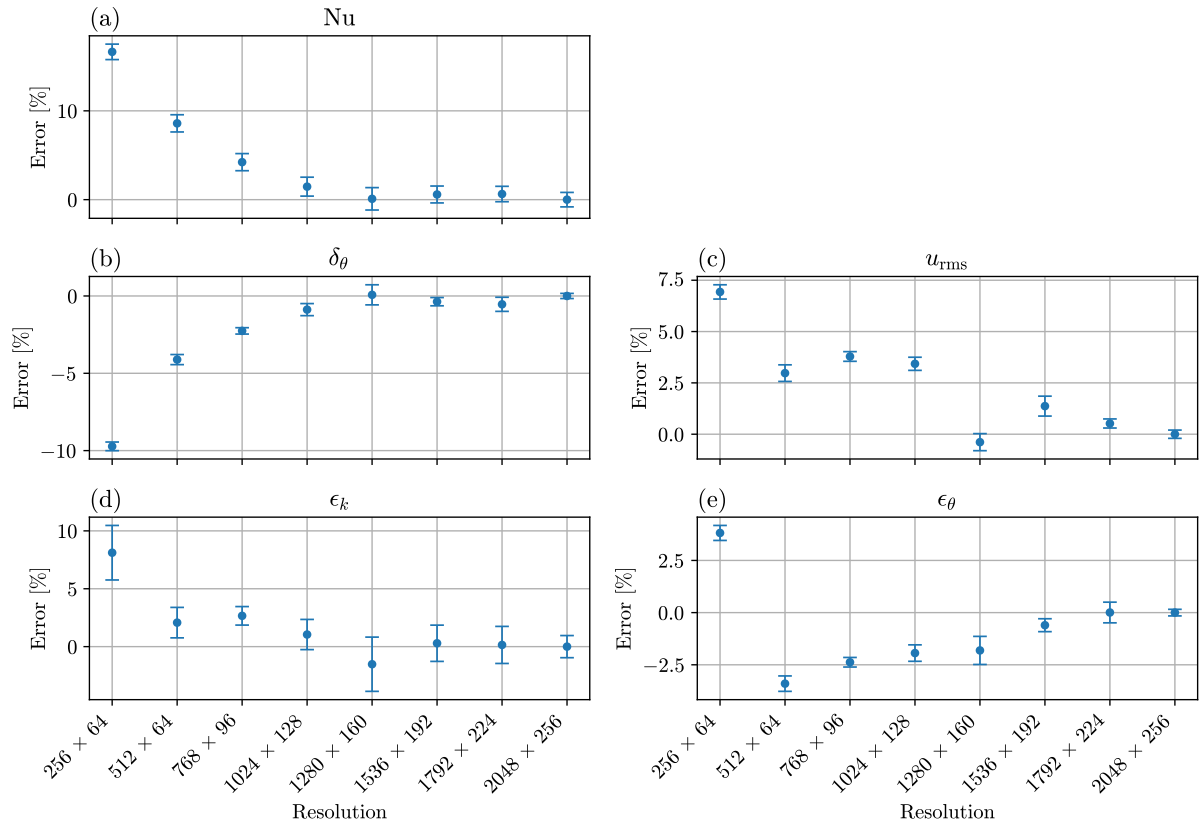


Figure 3.1: Time-averaged Nusselt number (a), thermal boundary layer thickness (b), RMS speed (c), kinetic energy dissipation rate (d) and thermal dissipation rate (e) as functions of model resolution, expressed as percentage errors relative to the values from the highest-resolution simulation (2048 × 256). Refer to the corresponding list items in the text for more detailed definitions of the quantities.

This page intentionally left blank

Bibliography

- Burns, K. J., G. M. Vasil, J. S. Oishi, D. Lecoanet, and B. P. Brown (2020). “Dedalus: a flexible framework for numerical simulations with spectral methods”. *Phys. Rev. Res.* **2**(2). DOI: [10.1103/PhysRevResearch.2.023068](https://doi.org/10.1103/PhysRevResearch.2.023068).
- Chandrasekhar, S. (1961). *Hydrodynamic and hydromagnetic stability*. Oxford: Clarendon Press. ISBN: 9780486319209.
- Chillà, F. and J. Schumacher (2012). “New perspectives in turbulent Rayleigh-Bénard convection”. *Eur. Phys. J. E* **35**(7). DOI: [10.1140/epje/i2012-12058-1](https://doi.org/10.1140/epje/i2012-12058-1).
- Grötzbach, G. (1983). “Spatial resolution requirements for direct numerical simulation of the Rayleigh-Bénard convection”. *J. Comput. Phys.* **49**(2). DOI: [10.1016/0021-9991\(83\)90125-0](https://doi.org/10.1016/0021-9991(83)90125-0).
- Kooij, G. L., M. A. Botchev, E. M. A. Frederix, B. J. Geurts, S. Horn, D. Lohse, E. P. van der Poel, O. Shishkina, R. J. A. M. Stevens, and R. Verzicco (2018). “Comparison of computational codes for direct numerical simulations of turbulent Rayleigh-Bénard convection”. *Comput. Fluids* **166**. DOI: [10.1016/j.compfluid.2018.01.010](https://doi.org/10.1016/j.compfluid.2018.01.010).
- Le Quéré, P. (1991). “Accurate solutions to the square thermally driven cavity at high Rayleigh number”. *Comput. Fluids* **20**(1). DOI: [10.1016/0045-7930\(91\)90025-D](https://doi.org/10.1016/0045-7930(91)90025-D).
- Lord Rayleigh (1916). “On convection currents in a horizontal layer of fluid, when the higher temperature is on the under side”. *Philos. Mag.* **32**(192). DOI: [10.1080/14786441608635602](https://doi.org/10.1080/14786441608635602).
- Ouertatani, N., N. Ben Cheikh, B. Ben Beya, and T. Lili (2008). “Numerical simulation of two-dimensional Rayleigh-Bénard convection in an enclosure”. *C.R. Mec.* **336**(5). DOI: [10.1016/j.crme.2008.02.004](https://doi.org/10.1016/j.crme.2008.02.004).
- Pope, S. B. (2000). *Turbulent flows*. Cambridge: Cambridge University Press. ISBN: 9780521598866. DOI: [10.1017/CB09780511840531](https://doi.org/10.1017/CB09780511840531).
- Scheel, J. D., M. S. Emran, and J. Schumacher (2013). “Resolving the fine-scale structure in turbulent Rayleigh-Bénard convection”. *New J. Phys.* **15**(11). DOI: [10.1088/1367-2630/15/11/113063](https://doi.org/10.1088/1367-2630/15/11/113063).
- Shishkina, O., R. J. A. M. Stevens, S. Grossmann, and D. Lohse (2010). “Boundary layer structure in turbulent thermal convection and its consequences for the required numerical resolution”. *New J. Phys.* **12**(7). DOI: [10.1088/1367-2630/12/7/075022](https://doi.org/10.1088/1367-2630/12/7/075022).
- Stevens, R. J. A. M., R. Verzicco, and D. Lohse (2010). “Radial boundary layer structure and Nusselt number in Rayleigh-Bénard convection”. *J. Fluid Mech.* **643**. DOI: [10.1017/S0022112009992461](https://doi.org/10.1017/S0022112009992461).
- Verzicco, R. and R. Camussi (1999). “Prandtl number effects in convective turbulence”. *J. Fluid Mech.* **383**. DOI: [10.1017/S0022112098003619](https://doi.org/10.1017/S0022112098003619).